

# On the role of Mg content in $\text{Mg}_2(\text{Si},\text{Sn})$ : Assessing its impact on electronic transport and estimating the phase width by in situ characterization and modelling

Aryan Sankhla<sup>a,\*</sup>, Hasbuna Kamila<sup>a</sup>, Harshita Naithani<sup>a</sup>, Eckhard Mueller<sup>a,b</sup> and Johannes de Boor<sup>a,c,\*</sup>

<sup>a</sup>Institute of Materials Research, German Aerospace Center (DLR), Germany

<sup>b</sup>Institute of Inorganic and Analytical Chemistry, Justus Liebig University of Giessen, Giessen, Germany

<sup>c</sup>Institute of Technology for Nanostructures (NST), Faculty of Engineering, University of Duisburg-Essen, Germany

\*Corresponding authors: Aryan.Sankhla@dlr.de, Johannes.deBoor@dlr.de

<https://doi.org/10.1016/j.mtphys.2021.100471>

## Abstract

Carrier transport in  $\text{Mg}_2\text{Si}_{1-x}\text{Sn}_x$  thermoelectrics was experimentally found to be highly sensitive to high temperature heat treatment and in particular the role of the precise Mg content has been discussed controversially. Considering this, electrical transport properties of Sb doped  $\text{Mg}_2\text{Si}_{0.4}\text{Sn}_{0.6}$  were measured in-situ during annealing at 710 K. We measured two identical samples: sample 1, for the Seebeck coefficient and the electrical conductivity ( $\sigma$ ) measurement in helium, and sample 2 for Hall coefficient and  $\sigma$  measurement in vacuum, respectively. Both samples largely remain single phase and did not show de-mixing after annealing for  $\sim 276$  hours and  $\sim 1100$  hours respectively. The observed experimental data can be modelled using a single- and two parabolic band model and a continuous reduction in majority carriers is identified, which can be linked to Mg loss. Thorough analysis furthermore reveals mobility loss and a lowering of the density of states effective mass which could both be due to ongoing Mg loss or due to lifted degeneracy of conduction bands in  $\text{Mg}_2\text{Si}_{0.4}\text{Sn}_{0.6}$  at room temperature. Finally, we can link the change in carrier concentration to a change in Mg-related defects and identify a phase width  $\Delta\delta$  in  $\text{Mg}_{2-\delta}\text{Si}_{0.4}\text{Sn}_{0.6}$ .

## Introduction

Solid state power generation devices, fabricated using thermoelectric materials, directly convert heat to electricity and are a potentially sustainable and scalable solution to global energy requirements. The performance of any material to be used in a thermoelectric device is characterized by its thermoelectric figure-of-merit ( $zT$ ),  $zT = (S^2\sigma/\kappa)T$ , where  $S$  is the Seebeck coefficient,  $\sigma$  is the electrical conductivity,  $\kappa$  is the thermal conductivity (comprising contributions from lattice thermal conductivity ( $\kappa_{\text{lat}}$ ), electronic thermal conductivity ( $\kappa_{\text{ele}}$ ) and bipolar thermal conductivity ( $\kappa_{\text{bip}}$ )) and  $T$  is the absolute temperature, respectively<sup>1</sup>. An efficient thermoelectric material should have a high power factor ( $PF = S^2\sigma$ ) and a low (total) thermal conductivity.

Thermoelectric devices work at elevated temperatures in the range of 300 K – 1100 K, and their thermal stability at operating temperatures is a significant challenge to overcome. Therefore, it is important to understand the impact of heat treatment on the material for prolonged duration at operation temperatures.

Previous reports on different materials<sup>2-9</sup> studied effects of heat treatment by comparing phase constitution, microstructure and corresponding thermoelectric properties before and after heat treatment, and speculate on degradation mechanism qualitatively. Such studies have also been carried out for  $\text{Mg}_2\text{X}$  materials<sup>10, 11</sup> which are an attractive class of thermoelectrics featuring a low mass density, environmental compatibility, economic precursor elements and high thermoelectric performance<sup>12-14</sup>. However, there is no report of direct observation of change in materials properties during annealing which could provide us a better insight into degradation mechanism and affected parameters.

We therefore carried out annealing experiments utilizing n-type  $\text{Mg}_2\text{Si}_{0.4}\text{Sn}_{0.6}$  and measured electrical transport properties in-situ during the complete annealing duration. We specifically chose this composition since it possesses better thermoelectric properties, due to band convergence and low lattice thermal conductivity, compared to the binary end members ( $\text{Mg}_2\text{Si}$  and  $\text{Mg}_2\text{Sn}$ )<sup>15-18</sup>. Our in-situ measured transport properties showed a degradation with increasing annealing duration and a saturation after 210 hours of annealing. The room temperature Hall carrier concentration of sample 1 decreased by an order of magnitude after annealing compared to prior annealing. Previous studies on  $\text{Mg}_2\text{X}$  and its solid solutions report that the thermochemical stability, and the thermoelectric transport properties both are sensitive to the Mg content<sup>19-21</sup>. A variation in the Mg content particularly influences the limits of the miscibility gap and the degradation kinetics<sup>22</sup>. We also learn from our previous studies that varying the duration of the high temperature (700 °C) compaction step leads to Mg loss which causes a degradation of  $n$  and mobility ( $\mu$ )<sup>23-25</sup>. These observations are in accordance with the fact that the Mg content in the  $\text{Mg}_2\text{X}$  materials directly relates to the density of charged defects and therefore affects their electrical transport properties. With this knowledge of a sensitivity to Mg content of both degradation kinetics and transport properties, mainly at elevated temperatures, we analyzed the measured transport properties using single-/multiband transport models.

The analysis confirmed that an ongoing loss of  $n$  and  $\mu$  was responsible for degradation of corresponding transport properties during annealing. We also found that the material obeys single band transport for the first 80 hours of annealing at 710 K. Following this, a non-linear behavior of Seebeck coefficient during longer annealing durations (> 80 hours) affirmed minority carriers from the valence band influencing the transport, when analyzed using a two-band model. The change in  $n$  and corresponding properties can be attributed to Mg loss which favors formation of p-type defects. Furthermore, single band analysis on transport properties before and after annealing suggests a lowering of  $m_D^*$  which can be a consequence of either an offset between supposedly converged conduction bands or  $n$  loss (or Mg loss). The same reason(s) likely affects and increases electron-phonon interaction that leads to the observed loss of mobility.

## **Experimental Section**

$\text{Mg}_2\text{Si}_{1-x-y}\text{Sn}_x\text{Sb}_y$  ( $x = 0.6$ ,  $y = 0.015$ ) samples were synthesized using a high energy ball mill (SPEX 8000D Shaker Mill) followed by a direct current sinter pressing (DSP 510 SE, Dr. Fritsch GmbH, Fellbach, Germany) of the milled powders to obtain a compacted pellet. Particular details of the complete synthesis procedure are mentioned in<sup>16</sup>. Excess Mg (2 at. %), making a final composition  $\text{Mg}_{2.06}\text{Si}_{1-x-y}\text{Sn}_x\text{Sb}_y$ , was added to compensate for potential Mg loss during synthesis. The powder was sintered at a temperature of 973 K with a holding time of 20 min, in vacuum ( $\sim 10^{-5}$  bar), and under an external pressure/load of 67 MPa on the mold. The density of all the pellets was measured using the Archimedes method, with an error uncertainty in density measurements of  $\sim 1\%$ . The X-ray diffractograms of the sintered pellets were acquired utilizing a Bruker's D8-Advanced diffractometer in the  $2\theta$  range of  $20^\circ$ – $120^\circ$  with a step size of

0.01° using CuK $\alpha$  radiation (1.5406 Å). The microstructure was investigated by a Zeiss Ultra 55 system equipped with an energy dispersive X-ray (EDS) detector.

An in-situ annealing experiment was conducted on two samples utilizing in-house developed facilities for measuring temperature dependent transport properties<sup>26, 27</sup> at 710 K (~437 °C). The Seebeck coefficient and electrical conductivity of one sample were measured utilizing a four-probe technique during annealing under helium atmosphere. The helium atmosphere was maintained in an enclosed volume. On the other hand, the Hall coefficient  $R_H$  and the electrical conductivity of the second sample were measured during annealing by utilizing a van der Pauw configuration in vacuum under continuous pumping. The Hall voltage signals were acquired at different (but constant) magnetic field intensities with a maximum of  $\pm 0.5$  T. The Hall carrier concentration  $n_H$  was estimated from  $R_H$  assuming a single carrier type  $n_H = 1/R_H \cdot e$ . The thermal diffusivity ( $\alpha$ ) of both the samples was measured after the annealing experiment using a Netzsch LFA 467HT apparatus. The thermal conductivity ( $\kappa$ ) was obtained using the relation  $\kappa = \alpha \rho C_p$ , where  $\rho$  and  $C_p$  are the sample density and the heat capacity respectively. The  $C_p$  value was obtained from the Dulong-Petit limit for  $c_V^{DP}$ :  $C_p = c_V^{DP} + \frac{9E_t^2 T}{\beta_T \rho}$ ,  $E_t^{Mg_2Si_{0.4}Sn_{0.6}} \sim 1.7 \times 10^{-5} \text{ K}^{-1}$  and  $\beta_T^{Mg_2Si_{0.4}Sn_{0.6}} \sim 2.07 \times 10^{-11} \text{ Pa}^{-1}$  are the linear coefficient of thermal expansion and isothermal compressibility of  $Mg_2Si_{0.4}Sn_{0.6}$ , respectively<sup>28, 29</sup>. The temperature dependent thermal conductivity has been shown in Figure S1. The measurement error uncertainties for  $S$ ,  $\sigma$ ,  $\kappa$  and  $R_H$  are  $\pm 5\%$ ,  $\pm 5\%$ ,  $\pm 8\%$  and  $\pm 10\%$ , respectively. An overview of measurements conducted on each sample is tabulated (Table S1) in the supplementary information. The transport properties are analyzed assuming a single or two parabolic bands, using the governing equations<sup>30</sup> provided as equations S1-S13 in the supplementary information.

## **Results**

The X-ray diffractograms of the samples both before and after annealing experiments are shown in Figure 1a. These diffractograms show that samples are phase pure and crystallize in the *fcc* structure with *Fm* $\bar{3}m$  space group. The XRD data also affirms that the samples are microstructure-wise basically unaffected due to annealing. The lattice parameter of the samples before and after annealing, listed in Table 1, were predicted by Le Bail fitting using Chebychev's polynomials assuming that the samples were phase pure before and after annealing. The lattice parameters indicate negligible change in the stoichiometry of the material after annealing compared to before annealing. The microstructure was investigated to observe any change that might have occurred during the annealing experiment. A typical side effect of the employed synthesis route is a small fraction of Si-rich  $Mg_2(Si,Sn)$ , usually below the detection limit of XRD<sup>16, 31, 32</sup>. The area fraction of the secondary phase(s) in the sample before and after annealing was estimated to be ~2.5% (sample #2, before annealing) and ~2.3% (sample #1, after annealing) and ~2.6% (sample #2, after annealing, Figure S3) and hence remains stable. EDS analysis conducted on the samples before and after annealing are shown in Figures S2, S4 and S5 in the supplementary information. The analysis shows that the matrix composition after annealing is similar to the starting composition thus, the samples did not suffer Mg loss to an extent which could lead to de-mixing of the solid solution<sup>19, 22</sup>.

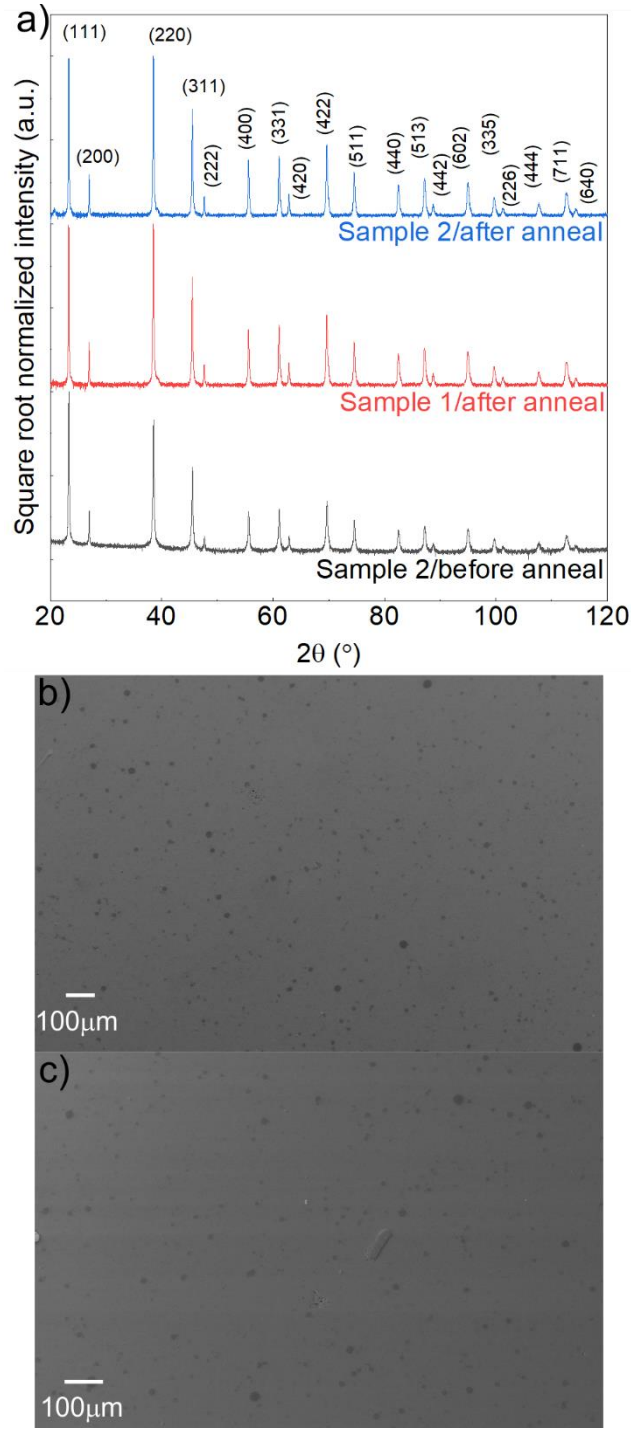


**Figure 1 a) X-ray diffractogram of sample 2 (before annealing), and sample 1 and sample 2 (after annealing). The diffractograms show that the samples are phase pure before and after annealing experiment, b) Low magnification secondary electron image of b) sample 2 before annealing, and c) sample 1 after annealing.**

Table 1 Room temperature Seebeck coefficient ( $S$ ), electrical conductivity ( $\sigma$ ), Hall carrier concentration ( $n_H$ ) and density of states effective mass ( $m_D^*$ ) predicted using a single parabolic band (SPB) model. The density and lattice parameter of both the

samples have also been tabulated below. Note that sample 1 was annealed in the S-sigma setup (setup 1) under He atmosphere while sample 2 was annealed in the Hall setup (setup 2) in vacuum.

Sample name		$S$ ( $\mu\text{V/K}$ )	$\sigma$ (S/cm)	$n_{\text{H}}$ ( $10^{20}$ ) ( $\text{cm}^{-3}$ )	$m_{\text{D}}^*(m_0)$	Sample density ( $\text{g/cm}^3$ )	Lattice parameter ( $\text{\AA}$ )
Sample 1 (setup 1)	Before annealing	-116	1888	2.45	2.4	3.00	-
	After annealing	-228	161.3	0.29	1.8	3.01	6.608(0)
Sample 2 (setup 2)	Before annealing	-111	1944	2.3	2.4	2.94	6.608(9)
	After annealing	-119.5	1305.2	1.7	2.05	2.98	6.609(3)

As a reference, we made both X-ray and SEM investigation on sample 2 before the annealing experiment. This comparison is reasonable since both samples were prepared using an identical, established synthesis route and showed similar thermoelectric properties at room temperature, listed in Table 1.

### **Measurement of transport properties on both samples**

The Seebeck coefficient and electrical conductivity of sample 1 were measured in-situ during annealing at 437 °C for ~275 hours under helium atmosphere. The temperature was already stabilized before initiating the annealing experiment. Before onset of annealing, during heat-up ramp, the temperature dependent transport properties were measured on this sample as shown in Figure S6. Broadly, the (annealing) time dependent Seebeck coefficient can be divided into 3 parts as shown in Figure 2(a). The first part is from the beginning of annealing experiment until ~80 hours of annealing, in which the Seebeck coefficient changes linearly. The second part ranges from 80 hours until 210 hours where the Seebeck coefficient varies non-linearly. Finally, for  $t > 210$  hours, the sample shows a nearly constant value of the Seebeck coefficient suggesting saturation. A decrease of the Seebeck coefficient (in absolute values) after a unidirectional increase (0 h – 80 h) between 80 hours to 210 hours indicates contribution of minority charge carriers to the transport. On the other hand, the electrical conductivity (Figure 2b) shows a continuous decay with annealing duration and saturates in the range of 165 – 175 S/cm. The different time dependence of the Seebeck coefficient and the electrical conductivity in the second region (80 h – 210 h) suggests that the degradation of transport properties is not only due to a probable carrier loss but carrier mobility might also be affected. The transport properties were fitted using a 5<sup>th</sup> order polynomial which is used as ‘measured’ data for later discussion and for transport modelling. The carrier concentration and electrical conductivity of sample 2 were measured during annealing under vacuum utilizing a high temperature Hall system. The temperature was stabilized prior to initiation of the annealing experiment.

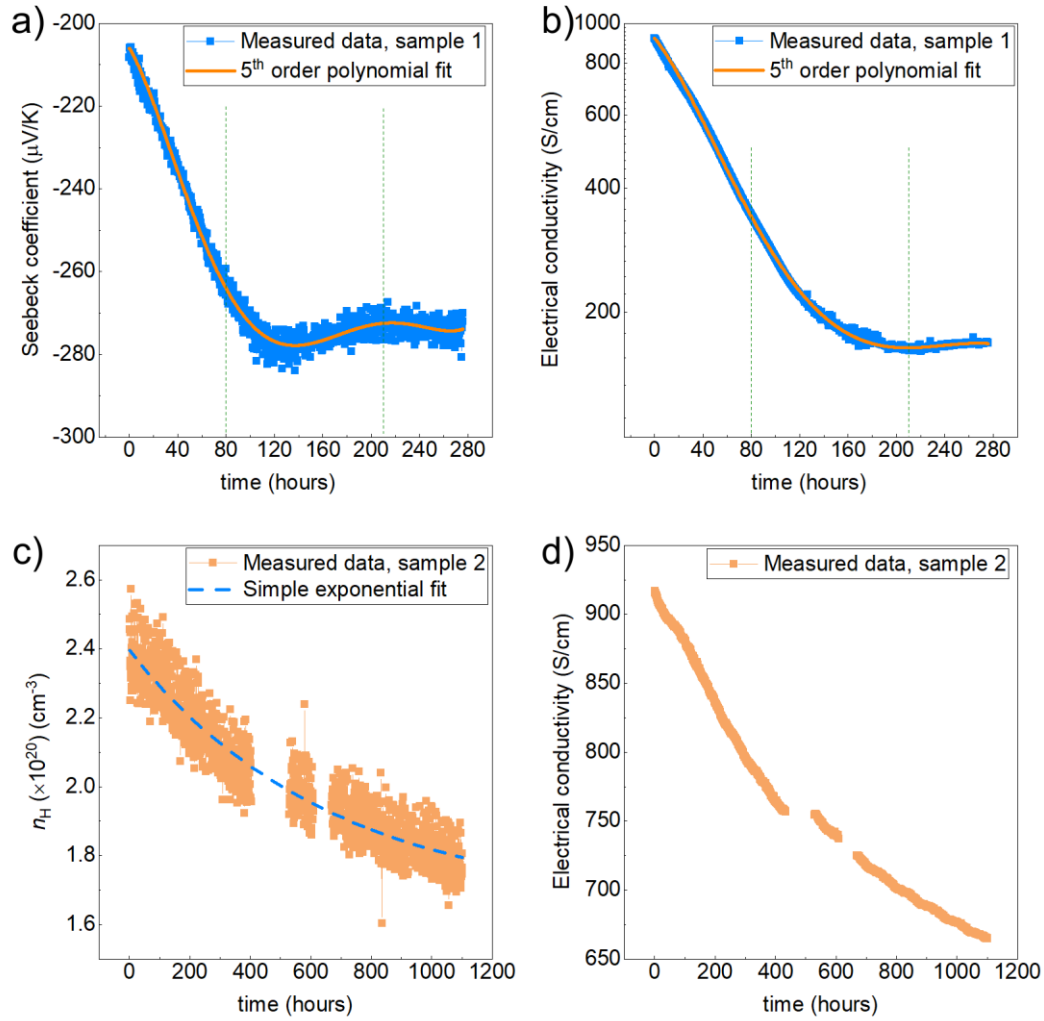


**Figure 2** a) Seebeck coefficient and b) electrical conductivity of sample 1, and c) Hall carrier concentration and d) electrical conductivity of sample 2, both measured in-situ during annealing at 710 K for a duration of nearly 275 hours, and over 1000 hours respectively. Note that the scale of y-axis in Figure 2b is logarithmic.

Transport properties of sample 2 were measured during heat-up ramp until the sample reached the desired annealing temperature as shown in Figure S7. As shown in Figure 2c and 2d, the complete annealing experiment took over 1000 hours however, the transport properties did not saturate. Besides, the measurement failed a couple of times during this experiment; once around 430 hours, and then in the range of 600-650 hours. We tested different temperatures for the purpose of optimization of the in-situ annealing experiment before conducting final annealing experiment. The transport properties of this optimization are shown in Figure S8 and indicate that changes in the thermoelectric properties occur drastically slower at temperatures below 710 K.

## Discussion

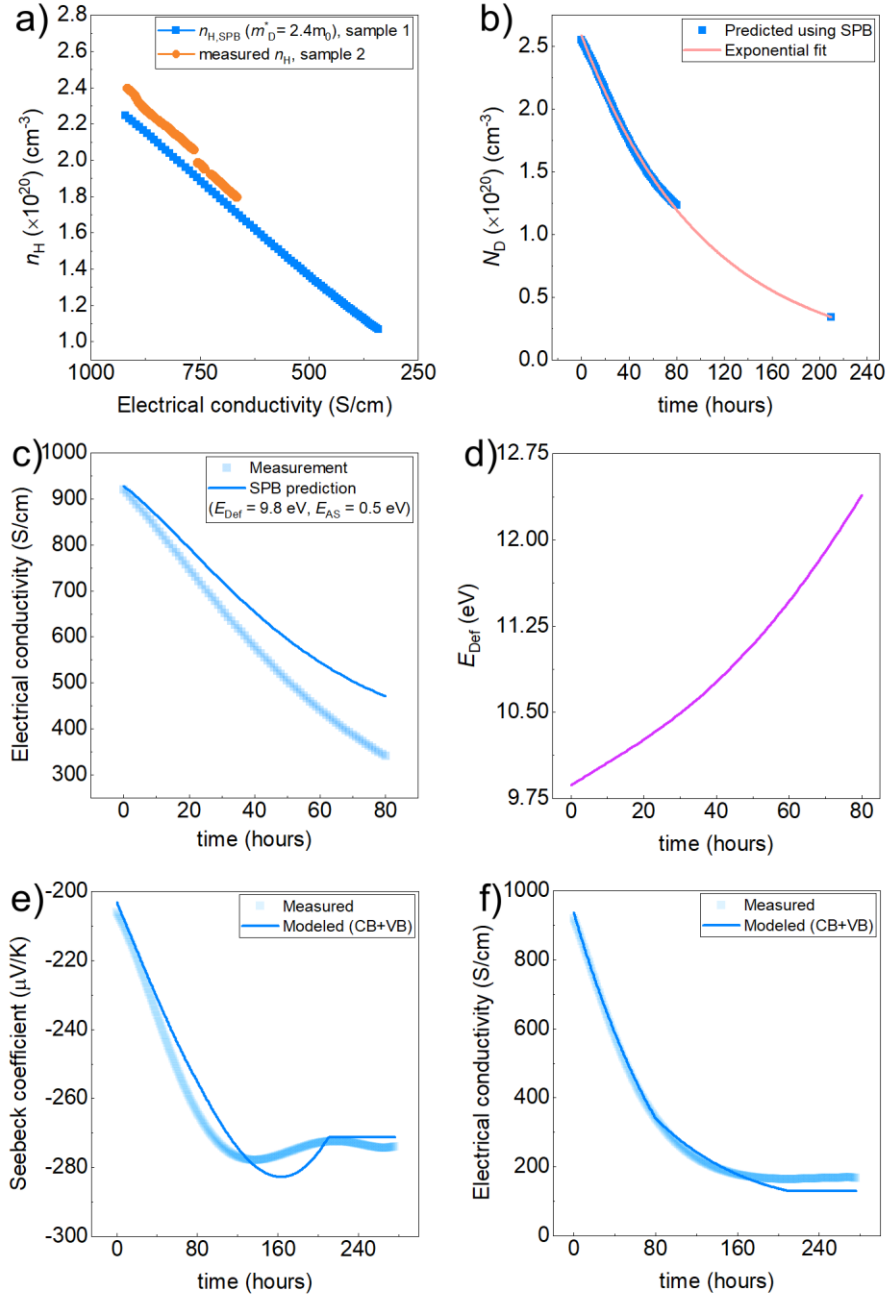
X-ray and SEM investigations on the samples before and after annealing suggest that they are essentially single phase with no indications of phase separation or elemental Si/Sn, and no significant change in area fraction of the secondary phase (Si-rich  $\text{Mg}_2(\text{Si},\text{Sn})$ ). The EDS analysis and diffractograms also suggest that after a possible Mg loss the samples remain within the phase width of  $\text{Mg}_2\text{Si}_{0.4}\text{Sn}_{0.6}$  (with respect to Mg content). This agrees with earlier reports<sup>22, 33</sup>, which suggest that stability is not unexpected if Mg loss can be controlled. The observed Si-rich  $\text{Mg}_2(\text{Si},\text{Sn})$  inclusions are expected to have a lower carrier concentration than the matrix<sup>32</sup> and furthermore form isolated islands. Thus, the fact that the material shows no observable change from the XRD and SEM analysis allows us to analyze the in-situ measured properties using a single-phase material model with material parameters that are assumed to be constant, except those related to the electrical transport.

Figure 3a shows the Hall carrier concentration as function of the electrical conductivity for both samples. Note that for sample 2 this is a direct result of the Hall measurement, while for sample 1 it is calculated using the SPB model and the measured Seebeck coefficient assuming a constant  $m_D^* = 2.4 m_0$  and using Equations S1-S4. We find a close agreement between  $n_H(\sigma)$  of both samples which indicates that our assumption of single band transport assuming a constant  $m_D^*$  is reasonable.

Besides, we also learn that the rate of change of the transport properties differs between the two employed setups and probably depends on annealing atmosphere. At  $T = 710$  K, the properties degraded slowly in vacuum ( $\sim 10$  times slower) compared to the experiment for sample 1 in the other setup in He atmosphere. The transport properties ( $S$  and  $\sigma$ ) (Figure S9) of a fresh sample, with a composition identical to sample 1 and 2, was monitored during in-situ annealing in vacuum (instead of He) to assess the influence of different atmospheres. The properties saturated after  $\sim 250$  hours of annealing, similar to experiment in He, indicating that atmosphere itself is not the main reason for the observed differences between the setups. Anyways, the same general dependence, as shown in Figure S10, suggests that the mechanism of degradation is quite similar. It also supports the idea to use data of both measurements combinedly, even if the decay has a different rate, as they have the electrical conductivity as common property. As sample 1 shows the faster and more complete change of properties we'll mainly exploit that in the following.

We utilized the measured Seebeck coefficient (Figure 2a) from the first part of the annealing (0 to 80 hours) experiment, where the values increase linearly with time, to estimate  $n$  using a constant  $m_D^*$  (Table 1) by employing a single parabolic band (SPB) model as shown in Figure 3(b). The relevant equations of the SPB model are mentioned in the SI. This is a reasonable assumption since the temperature dependent measured Seebeck coefficient agrees well with the predicted one on using said  $m_D^*$ , as shown in Figure S6 in supplementary information. The electrical conductivity was analyzed with the dependence of the mobility parameter on (annealing) duration assuming acoustic phonon (AP) and alloy scattering (AS) of charge carriers implemented in the model since AP is most relevant scattering mechanism at high temperatures, and AS is a relevant mechanism for solid solutions<sup>34, 35</sup>. The experimental and predicted electrical conductivity (assuming  $E_{\text{Def}} = 9.8$  eV and  $E_{\text{AS}} = 0.5$  eV, and using the predicted  $n$ ) agree well in the beginning, however, there is an increasing disagreement with time as shown in figure 3c. This suggests that the observed decrease of electrical conductivity is caused not only by a reduction in  $n$  but also by a reducing carrier mobility. Correspondingly, we tuned the electron-phonon interaction potential constant ( $E_{\text{Def}}$ ) (Figure 3d), which has an inverse dependence with mobility (equation S7), to match the measured electrical conductivity (using equations S5-S10). Adjusting  $E_{\text{Def}}$  is reasonable within the SPB framework as there is no physical reason why the other scattering parameter  $E_{\text{AS}}$  could be affected, and it has been shown before that  $E_{\text{Def}}$  might be affected e.g. by strain<sup>23, 36-38</sup> probably occurring at a nm scale due to Mg loss. The other

physical constants in the mobility equations, e.g. the longitudinal speed of sound ( $v_l$ ) are expected to be relatively constant; for  $v_l$  it was recently shown that the temperature dependence is not too strong and the variation with composition is not significant for small possible changes<sup>39</sup>. Beyond 80 hours, we observe a bending and a maximum in the absolute value of Seebeck coefficient (Figure 2a) which can be attributed to the influence of the minority carriers from the valence band, visualizing the SPB model does not hold (anymore).



**Figure 3** a) Hall carrier concentration ( $n_H$ ) of sample 1 and 2 as a function of electrical conductivity. The relative disagreement between  $n_H$  of both samples is  $\sim 10\%$ . Time dependent b) change in carrier (or dopant) concentration ( $N_D$ ), c) measured and predicted electrical conductivity (with  $E_{Def} = 9.8 \text{ eV}$ ,  $E_{AS} = 0.5 \text{ eV}$ ) until first 80 hours of annealing.



The discrepancy can be removed by tuning  $E_{Def}$  as a fitting parameter as shown in (d), time dependent predicted and experimental e) Seebeck coefficient, and f) electrical conductivity of sample 1. The Seebeck coefficient and electrical conductivity were predicted using a 2 parabolic band model (1CB and 1VB), using the parameters listed in Table 2.

Consequently, we have utilized a two parabolic band (2PB) model (relevant equations in SI) to capture the behavior of transport properties. For the prediction of transport properties using a 2PB model, solving the charge neutrality equation  $n_D^+ + p = n_A^- + n$  is required, where  $n$  and  $p$  are thermal equilibrium concentrations of electrons and holes while  $n_D^+$  is the (positive) charge carrier concentration due to donor atoms and  $n_A^-$  is the charge carrier concentration due to ionized acceptor atoms. In case of a single, fully ionized n-type dopant  $n_D^+$  is identical to the atomic concentration of that dopant, this is presumably the case here for Sb. However, in  $Mg_2(Si,Sn)$ , intrinsic defects are known to be crucial as well<sup>40, 41</sup> with excess Mg contributing to  $n_D^+$  in the form of interstitial defect  $I_{Mg}^{2+}$  and deficient Mg contributing to  $n_A^-$  in the form of vacancies  $V_{Mg}^{2-}$ . The  $n_D^+$  due to Sb can be assumed to be constant based on our last study<sup>23</sup>, however the net carrier concentration due to point defects  $N_D = n_{D,Sb}^+ + n_{D,Mg}^+ - n_{A,Mg}^-$  depends on Mg content in the material and changes if the Mg content changes.  $N_D$  might be called “dopant concentration” but note that this corresponds to an effective charge carrier concentration due to intrinsic and extrinsic point defects, rather than an atomic concentration. The charge neutrality equation can then be written as  $N_D + p = n$  and a value of  $N_D$  must be provided to solve it for the 2 band model.

For the single band analysis with one dominant carrier type, we can assume  $p \sim 0$  and  $N_D = n$ . We use this  $N_D$  for the first region (0 h – 80 h), however, we lack values beyond this duration. For this reason, we measured  $R_H(T)$  of sample 1 (Figure S11c) after the saturation of transport properties during annealing experiment. The measured  $R_H$  is nearly constant from room temperature up to  $\sim 500$  K while it decreases rapidly beyond this temperature due to the minority charge carrier contribution. The latter agrees with the prior  $S$  and  $\sigma$  measurements which also showed minority carrier contributions after the initial 80 h. The constant Hall coefficient for  $T < 500$  K indicates that below 500 K the majority charge carriers are dominant, the SPB model is valid and hence  $n = N_D$ . Consequently,  $n$  at room temperature after the annealing experiment can be assumed to be  $N_D$  at the end of our annealing experiment (at 276 h) i.e.  $N_{RT} = 0.34 \times 10^{20} \text{ cm}^{-3} = N_{D,276h}$ .

From Figure 2a, we learn that the Seebeck coefficient saturates from 210 hours and beyond, thus,  $N_D$  for this third region is assumed constant i.e.  $N_{D,sat} = 0.34 \times 10^{20} \text{ cm}^{-3}$ . It is plausible that the change in  $N_D$  is related to Mg loss and one can therefore expect  $N_D(t)$  to be a monotonous function. We have therefore used a simple exponential decay ( $N_D(t) = 0.34 \times 10^{20} + Ae^{-t/\tau}$ ; with  $\tau = -103.84$  h) between 0 h and 210 h. Note that this simple exponential fit agrees very well with the measurement results available between 0 h and 80 h, see Figure 3b. Following this, the transport properties were predicted utilizing a 2PB model by employing equations S1-S13, and the parameters listed in Table 2.

Table 2 Parameters employed for single- and multi-band modelling of electrical transport properties

Parameters	Employed values	How obtained
Band gap ( $E_g$ ) (eV) at 710 K	0.33	Fitting experimental data
DOS effective mass, $m_D^*$ ( $\times m_0$ )	$m_{D,CB}^* = 2.4$ ; $m_{D,VB}^* = 1.54$	<sup>23, 35</sup> ; linear interpolation of $m_D(x)$ for p- $Mg_2Si_{1-x}Sn_x$
Valley degeneracy ( $N_v$ )	$N_{v,CB} = 6$ ; $N_{v,VB} = 2$	<sup>35, 42</sup>

Atom density ( $N_0$ ) ( $m^{-3}$ )	$4.18 \times 10^{28}$	35
Longitudinal speed of sound ( $v_l$ ) (m/s)	5760	39
Fractional alloy composition ( $x$ )	0.6	-
Electron-phonon interaction potential constant ( $E_{Def}$ ) (eV)	0h to 80h: Fig 3d, 81 h to 276 h: 12.4	0h-80h: Predicted using SPB analysis on measured electrical conductivity data, for $t > 80h$ , $E_{Def,80h} = E_{Def>80h}$
Alloy scattering potential constant ( $E_{AS}$ ) (eV)	$E_{AS,CB} = 0.5$ , $E_{AS,VB} = 0.5$	35, 42
$N_D$ (Dopant concentration) ( $cm^{-3}$ )	Described in text	Figure 3b

Furthermore, the SPB validity range was confirmed by comparing the Seebeck coefficient according to the SPB and the 2PB model and evaluating  $1 - (\frac{S_{2PB}}{S_{SPB}})$ , see Figure S12 and the discussion there. The band gap value of  $E_g = 0.33$  eV closely agrees with values used by Bahk et al.<sup>43</sup> and Zhang et al.<sup>30</sup> suggesting our assumption of band gap is reasonable. We found reasonable but not perfect agreement between predicted and experimental Seebeck coefficient and electrical conductivity (Figure 3e and 3f). More specifically, our model reproduces the observed bending and non-linearity in Seebeck coefficient, but is shifted to longer annealing durations, and both predicted and measured electrical conductivity disagree moderately at longer annealing durations. An imperfect agreement can be due to a non-perfect estimation of  $N_D$  but could also be because we assume all other modelling parameters to be constant over the complete annealing duration. Furthermore, assuming one effective conduction band in a 2PB model to analyze transport properties might not be fully justified since each conduction band might have differential contribution to the transport as it is not clear how well the convergence is fulfilled. Our analysis and previous observations<sup>11</sup> furthermore suggest a lowering in  $m_D^*$  with annealing. This lowering can be qualitatively explained by a lifted degeneracy of the converged conduction bands for n-type  $Mg_{2-δ}Si_{0.385}Sn_{0.6}Sb_{0.015}$  and varying  $n$ <sup>44</sup>. The same reason could also explain an increase in  $E_{Def}$ , observed within the SPB analysis and shown in Figure 3d. The corresponding figures (S13 and S14) and a more detailed discussion is presented in the supplementary information. The observed changes in  $m_D^*$  could be a direct consequence of a change of the density of states due to annealing causing Mg loss or due to a minor offset between two conduction bands. Similarly, the deduced increase in  $E_{Def}$  could be due to an actual increase in the acoustic phonon scattering or an artifact from the SPB analysis on an actual 2 conduction band system. However, for a detailed understanding and confirmation of our modelling results, which reflect changes in said parameters, further experimental data is required.

Based on our last study<sup>23</sup>, some Mg loss might not be bad due to counteracting effects between  $\mu$  and  $\kappa_{lat}$  but large Mg loss clearly leads to poor electrical properties, as shown by the PF(T) (Figure S15 in supplementary information) measured before and after the annealing experiment which also agrees with Kato's observations<sup>25</sup>.

Following the notation from Kato et al.<sup>24</sup>, the equivalent Mg deficiency in  $Mg_{2-δ}Si_{0.385}Sn_{0.6}Sb_{0.015}$  ( $δ = (4y - na^3)/8$ ) at room temperature, was estimated for the sample before and after annealing, where

$y$  is the Sb content, and  $a$  is the lattice parameter. The equation is based on the assumption that each Sb atom provides one electron, each  $I_{\text{Mg}}^{2+}$  donates two electrons and each  $V_{\text{Mg}}^{2-}$  accepts two electrons; other defects are neglected based on their lower densities in  $\text{Mg}_2\text{Si}$  and  $\text{Mg}_2\text{Sn}$ <sup>40, 41</sup>. A negative value of ( $\delta < 0$ ) can be obtained for hyper-stoichiometric samples, which is reasonable due to the symmetrical charge of the most relevant defects. From this we can estimate a phase width  $\Delta\delta$  for the employed composition and temperature and find  $\Delta\delta \sim 0.008$  ( $-0.002 < \delta < 0.006$ ). It is plausible to assume  $\delta = -0.002$  as the hyper-stoichiometric limit as we started the synthesis with a significant Mg excess ( $\delta = -0.06$ ).  $\delta = 0.006$  (Figure S16) can be identified as lower limit from the transport model: for the saturation regime ( $t > 210$  h) we find that the Seebeck coefficient at 710 K is still highly sensitive to changes of  $N_D$  ( $N_D/n \approx 5$ ) and a reduction of  $N_D$  below  $0.34 \times 10^{20} \text{ cm}^{-3}$  would lead to a further reduction of the absolute values of  $S$ , see Figure S17. As this is clearly not observed (Figure 3), we can backwards conclude that  $N_D$  is indeed stable beyond 210 h and thus Mg loss has stopped. This also implies that the Mg-loss rate is a strong function of the Mg content in  $\text{Mg}_{2-\delta}\text{Si}_{0.385}\text{Sn}_{0.6}\text{Sb}_{0.015}$  and that Mg evaporates easier for ( $-0.002 < \delta < 0.006$ ) than for  $\delta > 0.006$ . This is highly plausible as  $\delta > 0.006$  can only be achieved by a degradation of the material and the formation of elemental secondary phases<sup>19, 22</sup>. Our result for  $\Delta\delta \sim 0.008$  ( $-0.002 < \delta < 0.006$ ) and that from Kato's work<sup>25</sup> for 1 mol. % Sb,  $\Delta\delta \sim 0.006$  ( $-0.002 < \delta < 0.004$ ), are in close agreement. The corresponding stoichiometries before and after annealing is  $\text{Mg}_{2.002}\text{Si}_{0.385}\text{Sn}_{0.6}\text{Sb}_{0.015}$  and  $\text{Mg}_{1.994}\text{Si}_{0.385}\text{Sn}_{0.6}\text{Sb}_{0.015}$ , respectively. The likewise change in carrier concentration ( $\Delta n$ ) due to annealing our case is  $\Delta n = 2.25 \times 10^{20} \text{ cm}^{-3}$ , and for Kato (for  $\text{Mg}_2(\text{Si}_{0.5}\text{Sn}_{0.5})_{0.99}\text{Sb}_{0.01}$ ) is  $\Delta n = 1.6 \times 10^{20} \text{ cm}^{-3}$ . The minor differences in  $\Delta\delta$  (and  $\Delta n$ ) might arise from differences in Sb content, annealing temperature, Si:Sn ratio and annealing environment, which was 500 °C, 50:50 and  $P_{\text{Mg}} \sim 0.1$  Pa in the latter case, respectively. We observe a clear change in the composition going from Mg rich to Mg poor stoichiometry in both cases. We also note that there is quite a difference between the deduced “actual” composition before annealing ( $\delta = -0.002$ ) and the nominal one ( $\delta = -0.06$ ), indicating that Mg is lost during the synthesis or can be incorporated into the materials without an influence on the thermoelectric properties, e.g. on the grain boundaries.

## **Conclusions**

We investigated in situ an effect of annealing on the electrical transport properties of Sb-doped  $\text{Mg}_2\text{Si}_{0.4}\text{Sn}_{0.6}$ . Two identical samples were annealed in two different atmospheres i.e. sample 1, for  $S$  and  $\sigma$  measurement under helium, and sample 2 for  $R_H$  and  $\sigma$  measurement in vacuum, respectively. The samples do not show de-mixing and remain almost single phase in both setups during annealing at 710 K for several 100 hours. However, both samples show clear signs of charge carrier loss, presumably due to Mg loss; in fact, the observed change in  $S$ ,  $\sigma$  and  $R_H$  can be well explained assuming continuous Mg loss which follows a simple exponential time dependence. In situ transport measurements thus allow for an estimation of the Mg-loss rate and the involved time constants ( $> 10^2$  hours for our conditions). An in-depth analysis of the transport data using a single parabolic conduction band model and a two parabolic band (conduction plus valence band) model reveals furthermore a decrease in carrier mobility with ongoing Mg loss and a reduced density of states effective mass. Both could be a consequence of the Mg loss itself or indicate that the two conduction bands in  $\text{Mg}_2\text{Si}_{1-x}\text{Sn}_x$  are not fully converged at room temperature for  $x = 0.6$ . Finally, we can estimate a lower and an upper limit for the Mg-content in  $\text{Mg}_2\text{Si}_{0.4}\text{Sn}_{0.6}$  and show that the Mg loss rate depends on the Mg content in the material. In summary, this work highlights the benefits of in-situ measurements and combined transport analysis as this allows for insight on materials degradation mechanisms and kinetics.

## **Acknowledgments**

We would like to gratefully acknowledge the endorsement from DLR Executive Board Members for Space Research and Technology and the financial support from the Young Research Group Leader Program. The authors would like to thank P. Blaschkewitz (DLR) for his continuous support with the thermoelectric measurements. The authors thank Prof. Titas Dasgupta (Department of Metallurgical Engineering and Materials Science, IIT Bombay) for insightful discussion on this study. The authors also thank Radhika Ravindra Deshpande and Léo Millerand for their help with Le Bail analysis on X ray diffractograms. The authors A.S., H.K. and H.N. would like to acknowledge financial support by the German Academic Exchange Service (Fellowship No. 247 and No. 403), while J.d.B. is partially funded by the Deutsche Forschungsgemeinschaft (DFG, German Research Foundation), project number 396709363.

## **Data Availability Statement**

The raw data required to reproduce these findings are available to download from [INSERT PERMANENT WEB LINK(s)]. The processed data required to reproduce these findings are available to download from [INSERT PERMANENT WEB LINK(s)].

## **References**

1. Liu, W.; Hu, J.; Zhang, S.; Deng, M.; Han, C.-G.; Liu, Y., New trends, strategies and opportunities in thermoelectric materials: A perspective. *Materials Today Physics* **2017**, *1*, 50-60.
2. Byrnes, J.; Mitchell, D. R. G.; Aminorroaya Yamini, S., Thermoelectric performance of thermally aged nanostructured bulk materials—a case study of lead chalcogenides. *Materials Today Physics* **2020**, *13*, 100190.
3. Shuai, J.; Mao, J.; Song, S.; Zhang, Q.; Chen, G.; Ren, Z., Recent progress and future challenges on thermoelectric Zintl materials. *Materials Today Physics* **2017**, *1*, 74-95.
4. Al Malki, M. M.; Qiu, Q.; Zhu, T.; Snyder, G. J.; Dunand, D. C., Creep behavior and postcreep thermoelectric performance of the n-type half-Heusler alloy  $\text{Hf}_{0.3}\text{Zr}_{0.7}\text{NiSn}_{0.98}\text{Sb}_{0.02}$ . *Materials Today Physics* **2019**, *9*, 100134.
5. Brož, P.; Zelenka, F.; Kohoutek, Z.; Vřešťál, J.; Vykoukal, V.; Buršík, J.; Zemanová, A.; Rogl, G.; Rogl, P., Study of thermal stability of  $\text{CoSb}_3$  skutterudite by Knudsen effusion mass spectrometry. *Calphad* **2019**, *65*, 1-7.
6. Smalley, A. L. E.; Kim, S.; Johnson, D. C., Effects of Composition and Annealing on the Electrical Properties of  $\text{CoSb}_3$ . *Chemistry of Materials* **2003**, *15* (20), 3847-3851.
7. Shang, H.; Liang, Z.; Xu, C.; Song, S.; Huang, D.; Gu, H.; Mao, J.; Ren, Z.; Ding, F., N-type  $\text{Mg}_3\text{Sb}_{2-x}\text{Bi}_x$  with improved thermal stability for thermoelectric power generation. *Acta Materialia* **2020**, *201*, 572-579.
8. Jiang, C.; Fan, X. A.; Feng, B.; Hu, J.; Xiang, Q.; Li, G.; Li, Y.; He, Z., Thermal stability of p-type polycrystalline  $\text{Bi}_2\text{Te}_3$ -based bulks for the application on thermoelectric power generation. *Journal of Alloys and Compounds* **2017**, *692*, 885-891.

9. Pi, J.-H.; Kwak, S.-G.; Kim, S.-Y.; Lee, G.-E.; Kim, I.-H., Thermal Stability and Mechanical Properties of Thermoelectric Tetrahedrite  $\text{Cu}_{12}\text{Sb}_4\text{S}_{13}$ . *Journal of Electronic Materials* **2019**, *48* (4), 1991-1997.
10. Zhang, L.; Chen, X.; Tang, Y.; Shi, L.; Snyder, G. J.; Goodenough, J. B.; Zhou, J., Thermal stability of  $\text{Mg}_2\text{Si}_{0.4}\text{Sn}_{0.6}$  in inert gases and atomic-layer-deposited  $\text{Al}_2\text{O}_3$  thin film as a protective coating. *Journal of Materials Chemistry A* **2016**, *4* (45), 17726-17731.
11. Yin, K.; Zhang, Q.; Zheng, Y.; Su, X.; Tang, X.; Uher, C., Thermal stability of  $\text{Mg}_2\text{Si}_{0.3}\text{Sn}_{0.7}$  under different heat treatment conditions. *Journal of Materials Chemistry C* **2015**, *3* (40), 10381-10387.
12. Ayachi, S.; Deshpande, R.; Ponnusamy, P.; Park, S.; Chung, J.; Park, S.; Ryu, B.; Müller, E.; de Boor, J., On the relevance of point defects for the selection of contacting electrodes: Ag as an example for  $\text{Mg}_2(\text{Si},\text{Sn})$ -based thermoelectric generators. *Materials Today Physics* **2021**, *16*, 100309.
13. Liu, W.; Tan, X.; Yin, K.; Liu, H.; Tang, X.; Shi, J.; Zhang, Q.; Uher, C., Convergence of Conduction Bands as a Means of Enhancing Thermoelectric Performance of n-Type  $\text{Mg}_2\text{Si}_{1-x}\text{Sn}_x$  Solid Solutions. *Physical Review Letters* **2012**, *108* (16), 166601.
14. Dasgupta, T.; Stiewe, C.; de Boor, J.; Müller, E., Influence of power factor enhancement on the thermoelectric figure of merit in  $\text{Mg}_2\text{Si}_{0.4}\text{Sn}_{0.6}$  based materials. **2014**, *211* (6), 1250-1254.
15. Zhu, Y.; Han, Z.; Jiang, F.; Dong, E.; Zhang, B.-P.; Zhang, W.; Liu, W., Thermodynamic criterions of the thermoelectric performance enhancement in  $\text{Mg}_2\text{Sn}$  through the self-compensation vacancy. *Materials Today Physics* **2021**, *16*, 100327.
16. Sankhla, A.; Patil, A.; Kamila, H.; Yasseri, M.; Farahi, N.; Mueller, E.; de Boor, J., Mechanical Alloying of Optimized  $\text{Mg}_2(\text{Si},\text{Sn})$  Solid Solutions: Understanding Phase Evolution and Tuning Synthesis Parameters for Thermoelectric Applications. *ACS Applied Energy Materials* **2018**, *1* (2), 531-542.
17. Sankhla, A.; Yasseri, M.; Kamila, H.; Mueller, E.; de Boor, J., Experimental investigation of the predicted band structure modification of  $\text{Mg}_2\text{X}$  (X: Si, Sn) thermoelectric materials due to scandium addition. **2019**, *125* (22), 225103.
18. de Boor, J.; Dasgupta, T.; Kolb, H.; Compere, C.; Kelm, K.; Mueller, E., Microstructural effects on thermoelectric efficiency: A case study on magnesium silicide. *Acta Materialia* **2014**, *77*, 68-75.
19. Yasseri, M.; Sankhla, A.; Kamila, H.; Orenstein, R.; Truong, D. Y. N.; Farahi, N.; de Boor, J.; Mueller, E., Solid solution formation in  $\text{Mg}_2(\text{Si},\text{Sn})$  and shape of the miscibility gap. *Acta Materialia* **2020**, *185*, 80-88.
20. Chen, L.; Jiang, G.; Chen, Y.; Du, Z.; Zhao, X.; Zhu, T.; He, J.; Tritt, T. M., Miscibility gap and thermoelectric properties of ecofriendly  $\text{Mg}_2\text{Si}_{1-x}\text{Sn}_x$  ( $0.1 \leq x \leq 0.8$ ) solid solutions by flux method. *Journal of Materials Research* **2011**, *26* (24), 3038-3043.
21. Jung, I.-H.; Kang, D.-H.; Park, W.-J.; Kim, N. J.; Ahn, S., Thermodynamic modeling of the Mg-Si-Sn system. *Calphad* **2007**, *31* (2), 192-200.
22. Yasseri, M.; Mitra, K.; Sankhla, A.; de Boor, J.; Müller, E., Influence of Mg loss on the phase stability in  $\text{Mg}_2\text{X}$  (X = Si, Sn) and its correlation with coherency strain. *Acta Materialia* **2021**, 116737.
23. Sankhla, A.; Kamila, H.; Kelm, K.; Mueller, E.; de Boor, J., Analyzing thermoelectric transport in n-type  $\text{Mg}_2\text{Si}_{0.4}\text{Sn}_{0.6}$  and correlation with microstructural effects: An insight on the role of Mg. *Acta Materialia* **2020**, *199*, 85-95.
24. Kato, D.; Iwasaki, K.; Yoshino, M.; Yamada, T.; Nagasaki, T., Significant effect of Mg-pressure-controlled annealing: non-stoichiometry and thermoelectric properties of  $\text{Mg}_{2-\delta}\text{Si}_{1-x}\text{Sb}_x$ . *Physical Chemistry Chemical Physics* **2018**, *20* (40), 25939-25950.
25. Kato, D.; Iwasaki, K., Mg-pressure-controlled annealing for tuning Mg content and thermoelectric properties of  $\text{Mg}_{2-\delta}(\text{Si}_{0.5}\text{Sn}_{0.5})_{1-x}\text{Sb}_x$ . *Journal of Alloys and Compounds* **2020**, 157351.
26. de Boor, J.; Stiewe, C.; Ziolkowski, P.; Dasgupta, T.; Karpinski, G.; Lenz, E.; Edler, F.; Mueller, E., High-Temperature Measurement of Seebeck Coefficient and Electrical Conductivity. *Journal of Electronic Materials* **2013**, *42* (7), 1711-1718.
27. de Boor, J.; Müller, E., Data analysis for Seebeck coefficient measurements. **2013**, *84* (6), 065102.

28. Pham, N. H.; Farahi, N.; Kamila, H.; Sankhla, A.; Ayachi, S.; Müller, E.; de Boor, J., Ni and Ag electrodes for magnesium silicide based thermoelectric generators. *Materials Today Energy* **2019**, *11*, 97-105.
29. Borup, K. A.; de Boor, J.; Wang, H.; Drymiotis, F.; Gascoin, F.; Shi, X.; Chen, L.; Fedorov, M. I.; Müller, E.; Iversen, B. B.; Snyder, G. J., Measuring thermoelectric transport properties of materials. *Energy & Environmental Science* **2015**, *8* (2), 423-435.
30. Zhang, L.; Xiao, P.; Shi, L.; Henkelman, G.; Goodenough, J. B.; Zhou, J., Suppressing the bipolar contribution to the thermoelectric properties of  $\text{Mg}_2\text{Si}_{0.4}\text{Sn}_{0.6}$  by Ge substitution. **2015**, *117* (15), 155103.
31. Kamila, H.; Goyal, G. K.; Sankhla, A.; Ponnusamy, P.; Mueller, E.; Dasgupta, T.; de Boor, J., Systematic analysis of the interplay between synthesis route, microstructure, and thermoelectric performance in p-type  $\text{Mg}_2\text{Si}_{0.2}\text{Sn}_{0.8}$ . *Materials Today Physics* **2019**, *9*, 100133.
32. de Boor, J.; Gupta, S.; Kolb, H.; Dasgupta, T.; Müller, E., Thermoelectric transport and microstructure of optimized  $\text{Mg}_2\text{Si}_{0.8}\text{Sn}_{0.2}$ . *Journal of Materials Chemistry C* **2015**, *3* (40), 10467-10475.
33. Farahi, N.; Stiewe, C.; Truong, D. Y. N.; de Boor, J.; Müller, E., High efficiency  $\text{Mg}_2(\text{Si},\text{Sn})$ -based thermoelectric materials: scale-up synthesis, functional homogeneity, and thermal stability. *RSC Advances* **2019**, *9* (40), 23021-23028.
34. Liu, X.; Zhu, T.; Wang, H.; Hu, L.; Xie, H.; Jiang, G.; Snyder, G. J.; Zhao, X., Low Electron Scattering Potentials in High Performance  $\text{Mg}_2\text{Si}_{0.45}\text{Sn}_{0.55}$  Based Thermoelectric Solid Solutions with Band Convergence. **2013**, *3* (9), 1238-1244.
35. Kamila, H.; Sahu, P.; Sankhla, A.; Yasseri, M.; Pham, H.-N.; Dasgupta, T.; Mueller, E.; de Boor, J., Analyzing transport properties of p-type  $\text{Mg}_2\text{Si}$ – $\text{Mg}_2\text{Sn}$  solid solutions: optimization of thermoelectric performance and insight into the electronic band structure. *Journal of Materials Chemistry A* **2019**, *7* (3), 1045-1054.
36. Murphy-Armando, F.; Fahy, S., Giant enhancement of n-type carrier mobility in highly strained germanium nanostructures. **2011**, *109* (11), 113703.
37. Lan, J.-L.; Zhan, B.; Liu, Y.-C.; Zheng, B.; Liu, Y.; Lin, Y.-H.; Nan, C.-W., Doping for higher thermoelectric properties in p-type  $\text{BiCuSeO}$  oxyarsenide. **2013**, *102* (12), 123905.
38. Liu, Z.; Wang, Y.; Mao, J.; Geng, H.; Shuai, J.; Wang, Y.; He, R.; Cai, W.; Sui, J.; Ren, Z., Lithium Doping to Enhance Thermoelectric Performance of  $\text{MgAgSb}$  with Weak Electron–Phonon Coupling. **2016**, *6* (7), 1502269.
39. Castillo-Hernandez, G.; Yasseri, M.; Klobes, B.; Ayachi, S.; Müller, E.; de Boor, J., Room and high temperature mechanical properties of  $\text{Mg}_2\text{Si}$ ,  $\text{Mg}_2\text{Sn}$  and their solid solutions. *Journal of Alloys and Compounds* **2020**, *845*, 156205.
40. Liu, X.; Xi, L.; Qiu, W.; Yang, J.; Zhu, T.; Zhao, X.; Zhang, W., Significant Roles of Intrinsic Point Defects in  $\text{Mg}_2\text{X}$  ( $\text{X} = \text{Si}, \text{Ge}, \text{Sn}$ ) Thermoelectric Materials. **2016**, *2* (2), 1500284.
41. Ryu, B.; Choi, E.-A.; Park, S.; Chung, J.; de Boor, J.; Ziolkowski, P.; Müller, E.; Park, S., Native point defects and low p-doping efficiency in  $\text{Mg}_2(\text{Si},\text{Sn})$  solid solutions: A hybrid-density functional study. *Journal of Alloys and Compounds* **2021**, *853*, 157145.
42. Liu, W.; Chi, H.; Sun, H.; Zhang, Q.; Yin, K.; Tang, X.; Zhang, Q.; Uher, C., Advanced thermoelectrics governed by a single parabolic band:  $\text{Mg}_2\text{Si}_{0.3}\text{Sn}_{0.7}$ , a canonical example. *Physical Chemistry Chemical Physics* **2014**, *16* (15), 6893-6897.
43. Bahk, J.-H.; Bian, Z.; Shakouri, A., Electron transport modeling and energy filtering for efficient thermoelectric  $\text{Mg}_2\text{Si}_{1-x}\text{Sn}_x$  solid solutions. *Physical Review B* **2014**, *89* (7), 075204.
44. Naithani, H.; Dasgupta, T., Critical Analysis of Single Band Modeling of Thermoelectric Materials. *ACS Applied Energy Materials* **2020**, *3* (3), 2200-2213.